

Supplemental Material: Altermagnetism in Two-Dimensional Ca_2RuO_4 perovskite

J. W. González,^{1,*} A.M León,^{2,3} C. González-Fuentes,⁴ and R. A. Gallardo⁵

¹*Departamento de Física, Universidad de Antofagasta,
 Av. Angamos 601, Casilla 170, Antofagasta, Chile*

²*Departamento de Física, Facultad de Ciencias, Universidad de Chile, Casilla 653, Santiago, Chile.*

³*Institute for Solid State and Materials Physics,
 TU Dresden University of Technology, 01062 Dresden, Germany*

⁴*Instituto de Física, Pontificia Universidad Católica de Chile, Vicuña Mackena 4860, 7820436 Santiago, Chile*

⁵*Departamento de Física, Universidad Técnica Federico Santa María, Avenida España 1680, Valparaíso, Chile*

(Dated: January 14, 2025)

SI. RELATION BETWEEN HUBBARD-U TERM AND GEOMETRY

Relationship between geometrical parameters and magnetic moment in Ruthenium atoms as a function of the Hubbard-U parameter, Table S1.

Magnetic conf.	a (Å)	a/b	Ru mag. (μ_B)	O in-plane mag. (μ_B)	O out-plane mag. (μ_B)
FM (U= 0 eV)	5.136	1.03	0.93	0.13	0.01
AF (U= 0 eV)	5.167	1.00	0.71	0.00	0.01
FM (U= 1 eV)	5.200	1.00	1.44	0.19	0.02
AF (U= 1 eV)	5.168	0.99	1.15	0.07	0.02
FM (U= 2 eV)	5.169	0.99	1.48	0.18	0.02
AF (U= 2 eV)	5.174	0.91	1.46	0.01	0.12
FM (U= 3 eV)	5.174	0.98	1.55	0.15	0.02
AF (U= 3 eV)	5.196	0.91	1.53	0.01	0.11

TABLE S1: Summary with the lattice constant (a), aspect ratio (a/b), Ruthenium magnetic moment, and Oxygen (in-plane and out-plane) magnetic moments as a function of the Hubbard-U term. The boldface labels indicate the ground state of each U value.

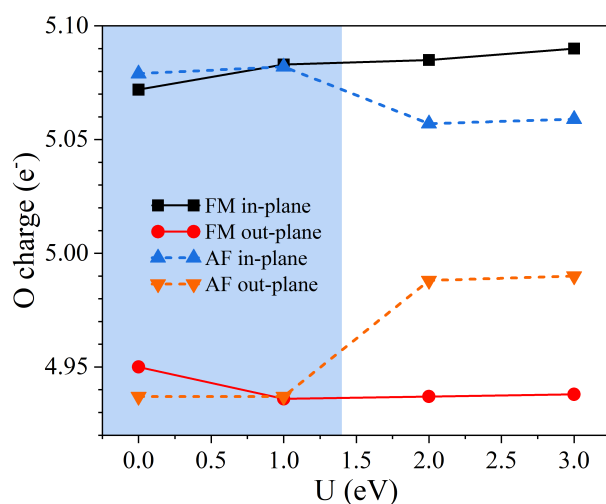


FIG. S1: Bader charges analysis for oxygen atoms (in e^-) as a function of the Hubbard U parameter for ferromagnetic (FM) and antiferromagnetic (AF) configurations, with both in-plane and out-of-plane magnetic orientations.

Bader charges analysis for oxygen atoms in Figure S1 data show that the oxygen charge slightly increases with U for FM configurations, with in-plane orientation exhibiting higher values than out-of-plane. In the AF case, the oxygen charge remains nearly constant for in-plane orientation but shows a distinct increase for the out-of-plane orientation as U increases. The shaded region indicates the range of U values used in the main calculations.

SII. ISING MODEL

In the two-dimensional Ising model used in this analysis, we consider periodic boundary conditions in a 30×30 supercell with a nearest-neighbor interaction described by the exchange constant J . $J > 0$ for ferromagnetic interaction, while $J < 0$ indicates antiferromagnetic interactions.

The energy of the system is given by:

$$E = -J \sum_{\langle i,j \rangle} \sigma_i \sigma_j,$$

where the sum is taken over all pairs of neighboring spins $\langle i,j \rangle$ and each lattice site is a spin variable $\sigma_{i,j} = \pm 1$

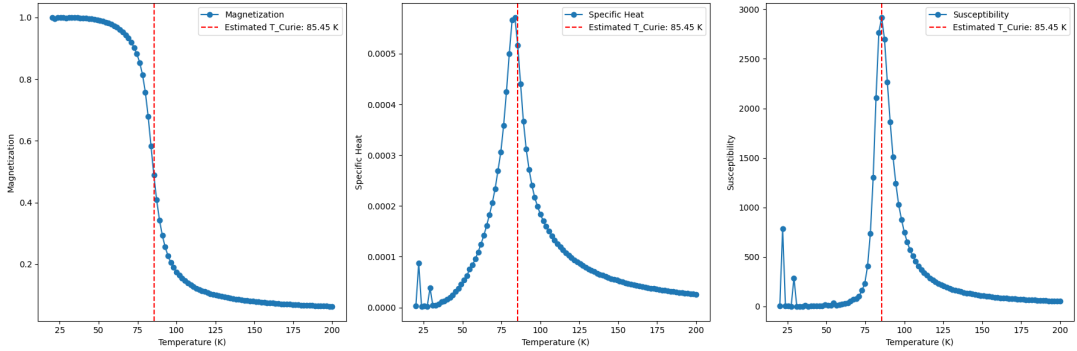


FIG. S2: (Color online) Ising model for an **FM system** with $J = 3.1$ meV: Magnetization, specific heat and susceptibility as a function of temperature.

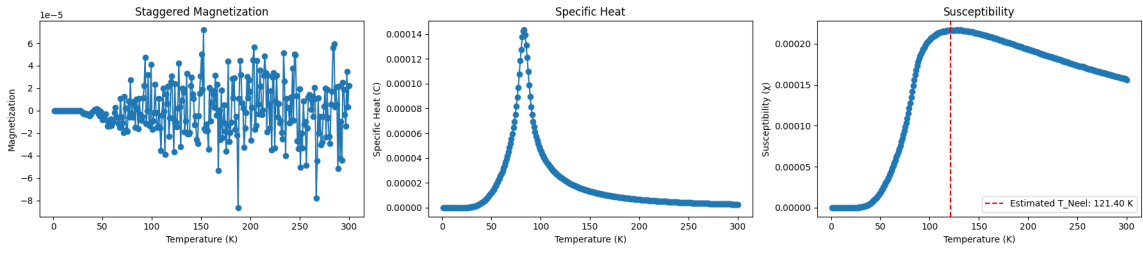


FIG. S3: (Color online) Ising model for an **AF system** with $J = -3.1$ meV: Magnetization, specific heat and susceptibility as a function of temperature.

We use Monte Carlo simulations using the Metropolis algorithm used to estimate physical quantities over a range of temperatures:

- A random spin is selected and flipped with a probability dependent on the change in energy, ΔE , given by:

$$\Delta E = -2J\sigma_{i,j} (\sigma_{i+1,j} + \sigma_{i-1,j} + \sigma_{i,j+1} + \sigma_{i,j-1}),$$

which represents the energy difference between the initial and proposed states.

- If $\Delta E < 0$, the spin is flipped unconditionally. Otherwise, the spin is flipped with probability:

$$P = \exp\left(-\frac{\Delta E}{k_B T}\right),$$

where k_B is the Boltzmann constant and T is the absolute temperature.

For each temperature, we let the system thermalize for 500 steps, and we take the average over the following 2000 simulation steps; later, we calculate the following observables:

Magnetization: Average absolute value of the total spin, normalized by the number of lattice sites,

$$M = \frac{\left| \sum_{i,j} \sigma_{i,j} \right|}{L^2},$$

where L is the lattice size.

Specific Heat: Derived from the energy fluctuations:

$$C = \frac{\langle E^2 \rangle - \langle E \rangle^2}{k_B T^2 L^2}.$$

Susceptibility: Derived from the magnetization fluctuations:

$$\chi = \frac{\langle M^2 \rangle - \langle M \rangle^2}{k_B T L^2}.$$

The Curie and Neél temperatures represent the critical temperatures at which ferromagnetic and antiferromagnetic materials undergo a phase transition to a paramagnetic phase, respectively.

On the one hand, in ferromagnetic systems, the Curie temperature is estimated from the temperature at which the magnetic susceptibility peaks. In Figure S2, we present averaged properties for the FM system. For $J = 3.10$ meV, the $T_C = 85.45$ K is closer to the reported values for similar systems¹.

On the other hand, in antiferromagnetic configuration, the Neél temperature is also estimated using the peak of the magnetic susceptibility. The AF calculations for $J = -3.10$ meV yields to $T_N = 121.4$ K; details are shown in Fig. S3.

SIII. AF BAND SPLITTING

In figure S4 we present the details of the highest occupied valence band, the left panel, correspond to the zoom of the band structure shown in Fig. 5(a). The right panel of Fig. S4 shows the energy difference between the up and down bands.

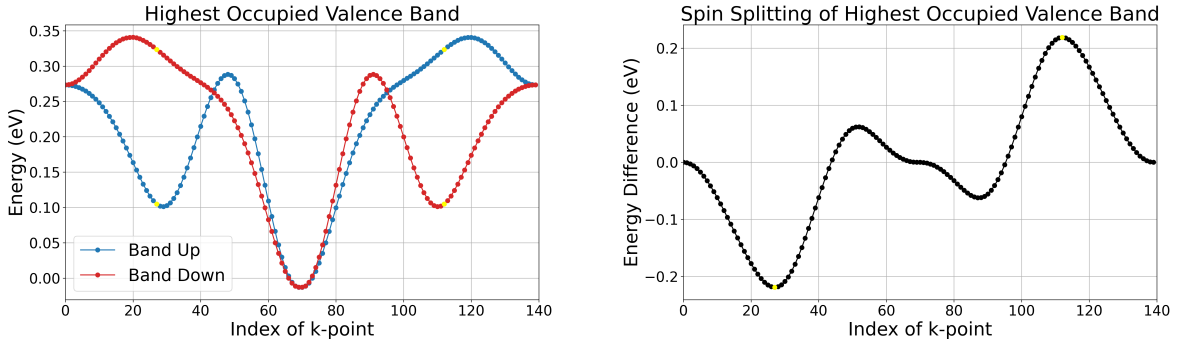


FIG. S4: (Color online) Detail of the highest occupied valence band V0 (without spin-orbit effects) along the $M'-\Gamma$ - M path for the antiferromagnetic ($U = 2$ eV) system.

SIV. LOCAL DENSITY OF STATES

The local density of states for the antiferromagnetic case with $U = 2$ eV, in Figure S5 shows that with and without spin-orbit coupling, the system is a semiconductor. The states near the Fermi level show a high contribution of orbitals from the Ruthenium and Oxygen atoms, favoring super-exchange interactions between the d-Ru and p-O orbitals.

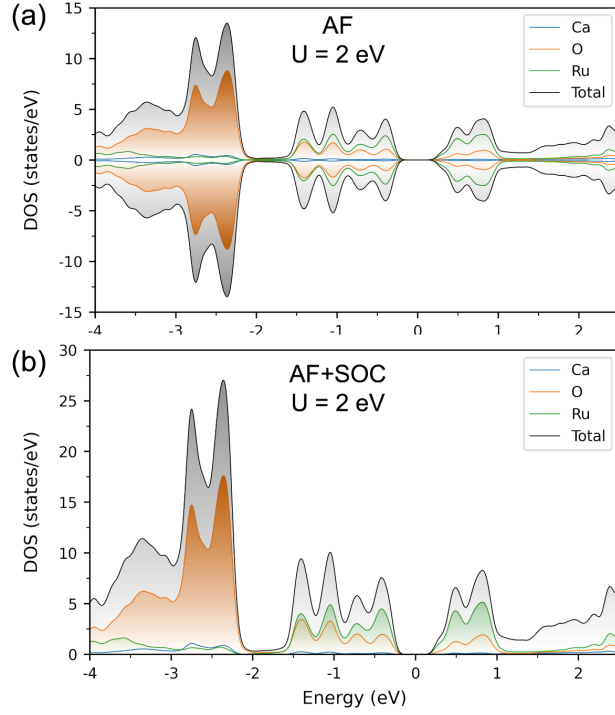


FIG. S5: (Color online) The density of states for the antiferromagnetic system with $U = 2$ eV. In (a) without spin-orbit and (b) with spin-orbit coupling. The colors represent the contribution of each atom.

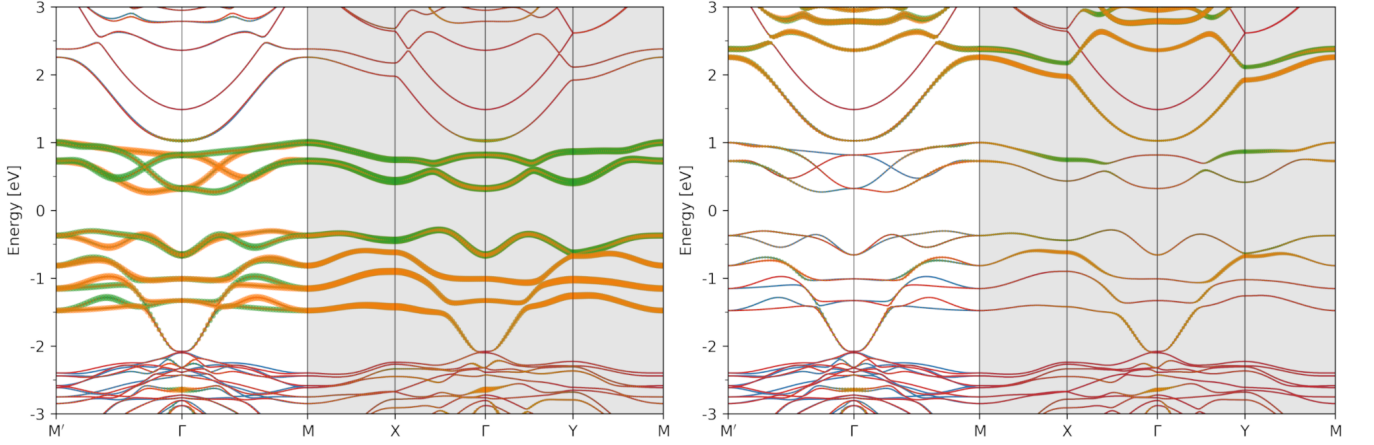


FIG. S6: Projected band structure for the antiferromagnetic system with $U = 2$ eV. The left panel shows the t_{2g} orbital projection, while the right panel shows the e_g orbital projection. The orange and green colors represent the contributions of different Ru atoms. The energy axis is referenced to the Fermi level at $E = 0$ eV. Note that this band structure corresponds to an extended path of Fig. 4(a) where the system only presents antiferromagnetic character along the $M' - \Gamma - M$ path.

SV. NON-COLLINEAR BAND STRUCTURE

In Fig. S7 we present the band structure along the $M' - \Gamma - M$ path for the antiferromagnetic system ($U = 2$ eV) with spin-orbit coupling, with magnetic moments projected along the x-axis (a), y-axis (b), and z-axis (c).

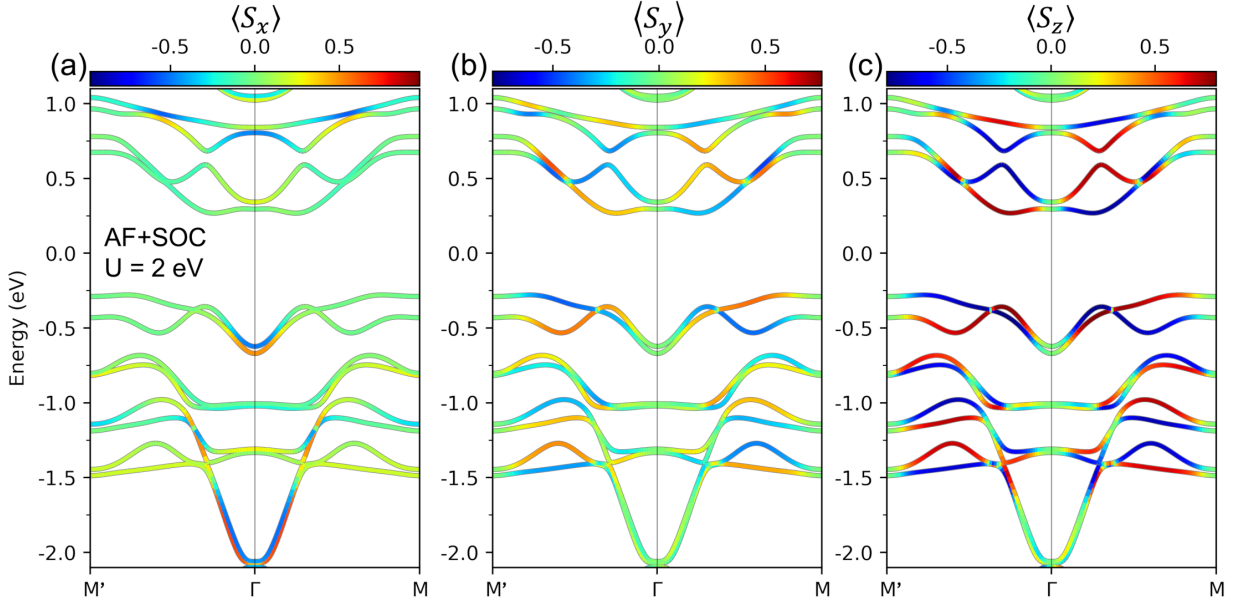


FIG. S7: (Color online) Projected band structure along the $M'-\Gamma-M$ path for the antiferromagnetic ($U = 2$ eV) system with spin-orbit coupling. The magnetic moments are projected along the (a) x-axis, (b) y-axis, and (c) z-axis. The color scale represents the expectation value of the spin component, with blue indicating negative values, red indicating positive values. Note the k-dependent band splitting and the differences in spin projection along each axis.

SVI. ELECTRIC FIELD

In this section, we explore the effect of an out-of-plane electric field (E_z) on the band structure and Berry curvature for the antiferromagnetic configuration ($U = 2$ eV) with spin-orbit coupling. We analyze the system for various electric field strengths: $E_z = 0.0$ eV/Å, $E_z = 0.5$ eV/Å, $E_z = 1.0$ eV/Å, and $E_z = 1.5$ eV/Å.

The band labeled 'C' is an e_g -band presents a higher sensibility to electric field. As E_z increases, this band stretches progressively to lower energies, eventually closing the energy gap near the Γ point. Fig. S8 shows the evolution of the band structure under different E_z values, while Figure 5(b) shows the reference band structure for $E_z = 0.0$ eV/Å.

Berry curvature summed over all occupied states in the k_x-k_y plane, in Figure S9, shows a clear evolution with increasing out-of-plane electric field (E_z). For $E_z = 0.0$ eV/Å, the Berry curvature distribution is symmetric with alternating positive and negative regions. As E_z increases, this symmetry is progressively broken, leading to more pronounced and localized regions of Berry curvature, particularly around the Γ point at $E_z = 1.5$ eV/Å.

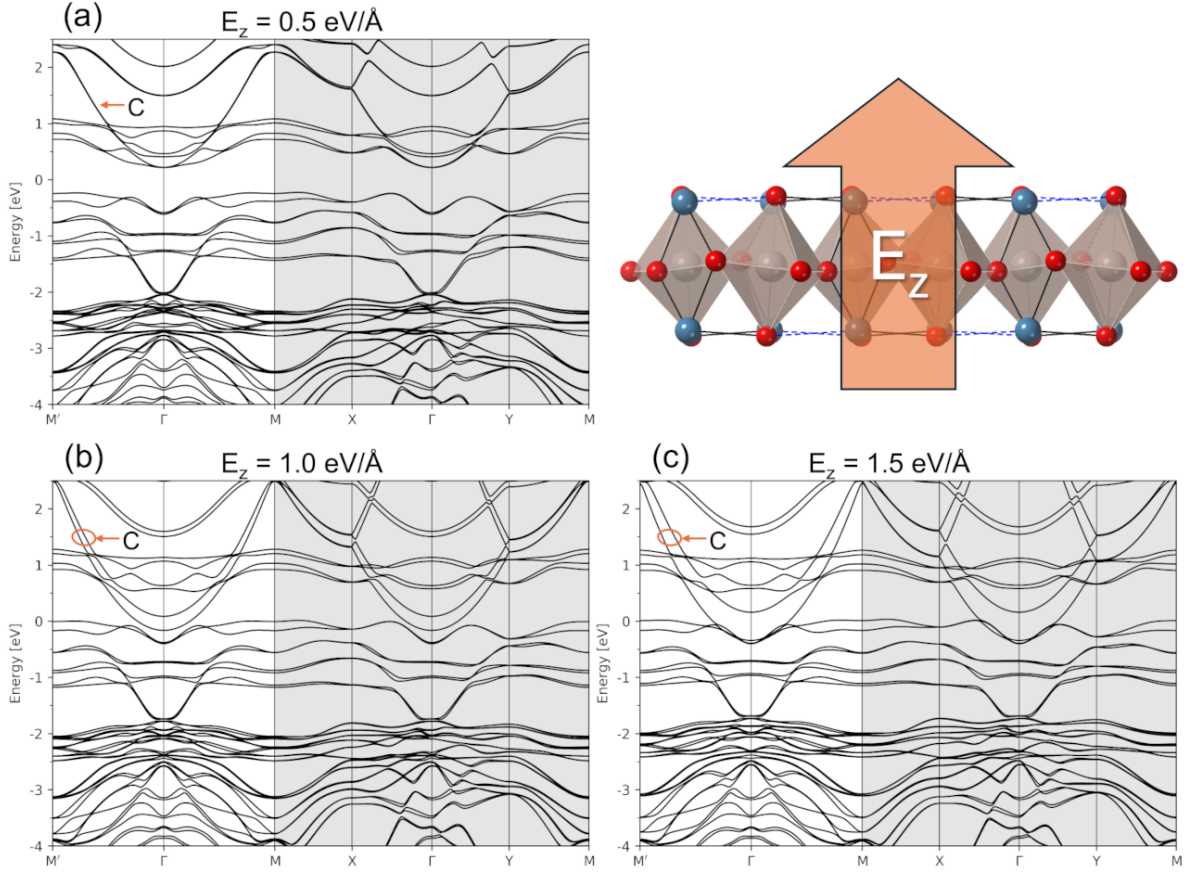


FIG. S8: Band structure for the antiferromagnetic configuration ($U = 2$ eV) with spin-orbit coupling under an out-of-plane electric field (E_z). Panel (a) correspond to $E_z = 0.5$ eV/Å, (b) $E_z = 1.0$ eV/Å, and (c) $E_z = 1.5$ eV/Å. The band structure for $E_z = 0.0$ eV/Å is shown in Fig. 5(b). The schematic shows the direction of the applied electric field relative to the 2D lattice.

SVII. MAGNETIC ANISOTROPY ENERGY (MAE)

After calculating the energy difference for the FM system (with spin-orbit effects) with the magnetic moment pointing in several directions, we have identified the easy axis along the z-direction and small in-plane anisotropy. Details in Figure S10.

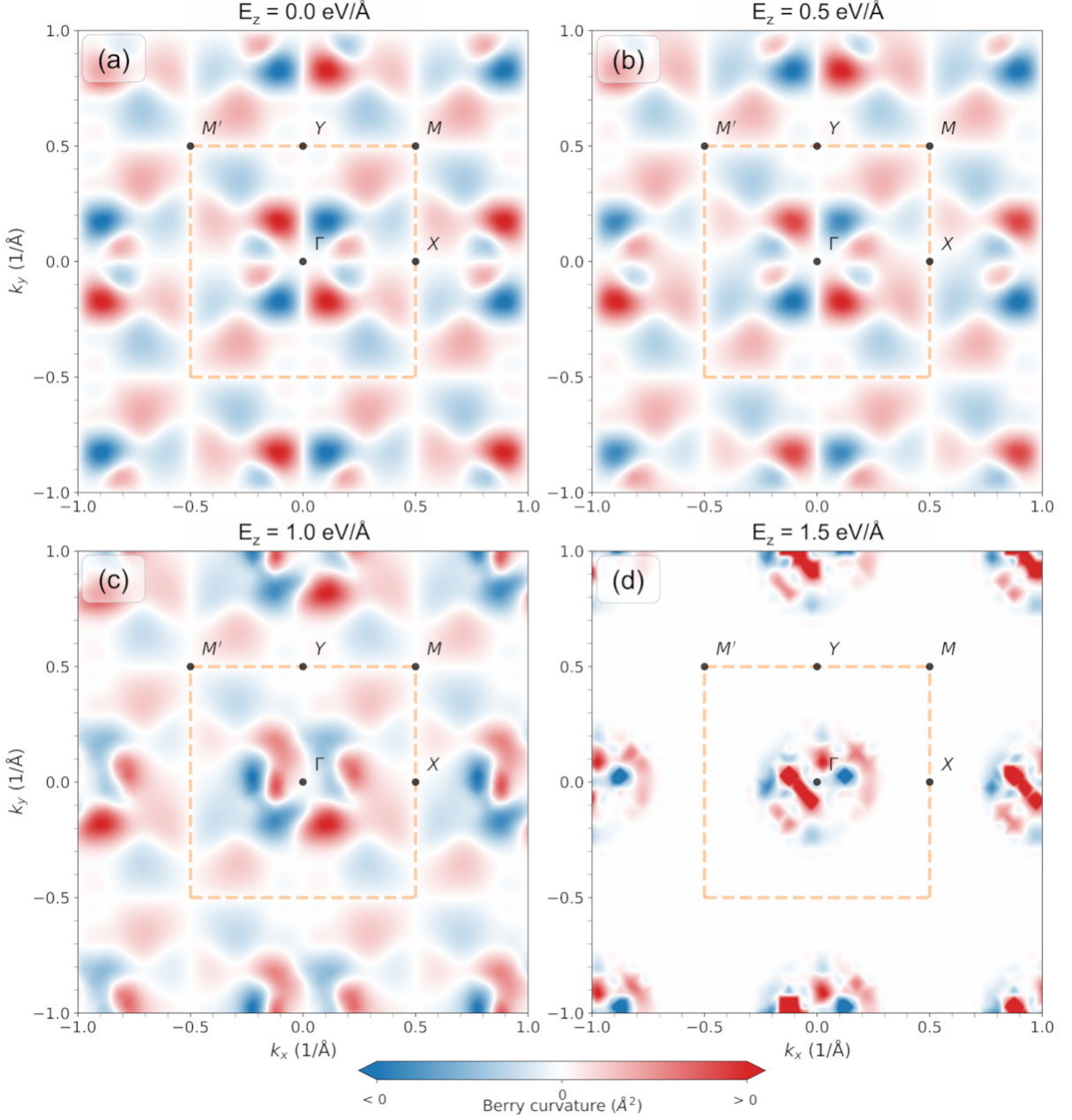


FIG. S9: Berry curvature summed over all occupied states in the k_x - k_y plane for the antiferromagnetic configuration ($U = 2$ eV) with spin-orbit coupling for out-of-plane electric fields (E_z). Panel (a) correspond to $E_z = 0.0$ eV/Å, (b) $E_z = 0.5$ eV/Å, (c) $E_z = 1.0$ eV/Å, and (d) $E_z = 1.5$ eV/Å. The dashed orange box outlines the first Brillouin zone, highlighting the high-symmetry points: Γ , X, M, Y, and M' . The blue and red areas represent negative and positive values of Berry curvature, respectively.

SVIII. TOY MODEL

As discussed in the main text, our toy model corresponds to the Ru-O plane of the 2D-CRO; we identify this core layer as the key component that generates the altermagnetic character of 2D-CRO. Figure S11 presents the symmetry operations responsible for such altermagnetic character. Note that the same symmetry operations apply to 2D-CRO, although it is more difficult to follow the results of the different operations.

In the first panel, we present our starting point, with four Oxygen atoms (depicted as red spheres) around each Ruthenium atom (green for the positive magnetic moment and orange for the negative magnetic moment). The second panel results from a time-reversal operation, corresponding to an inversion of the magnetic moments.

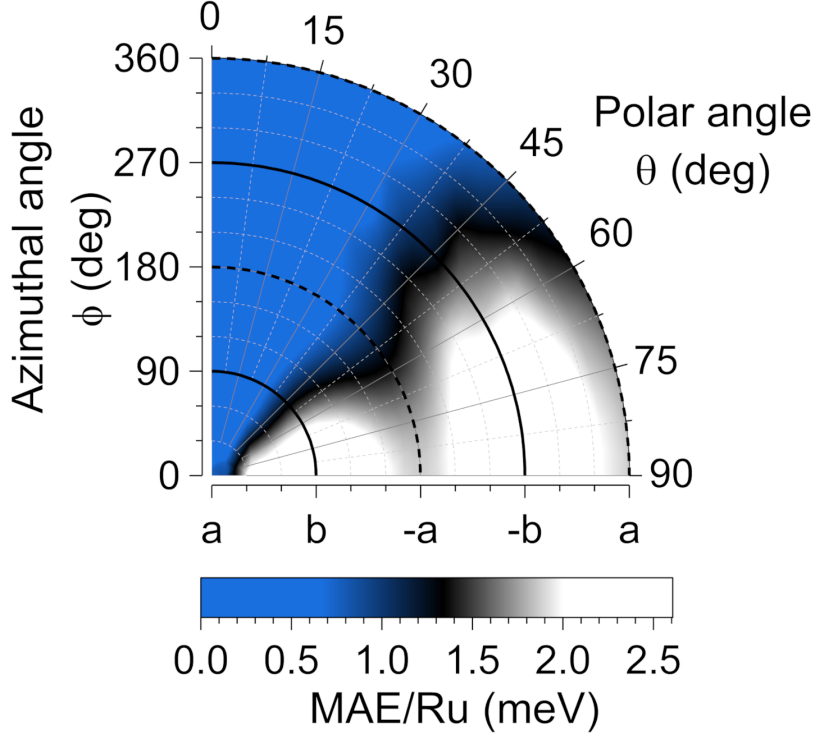


FIG. S10: (Color online) Magnetic anisotropy energy (MAE) of the ferromagnetic (FM) system ($U = 1$ eV) with spin-orbit coupling effects. The contour plot of the energy difference ($E(\theta, \phi) - E_{GS}$) per Ru atom as a function of the azimuthal angle (ϕ) and polar angle (θ) of the magnetic moment direction. The color scale represents the MAE, with blue indicating lower energy and white indicating higher energy. The ground state, corresponding to the magnetic moment pointing in the z-direction, is identified as the easy axis, and the system shows a small in-plane anisotropy.

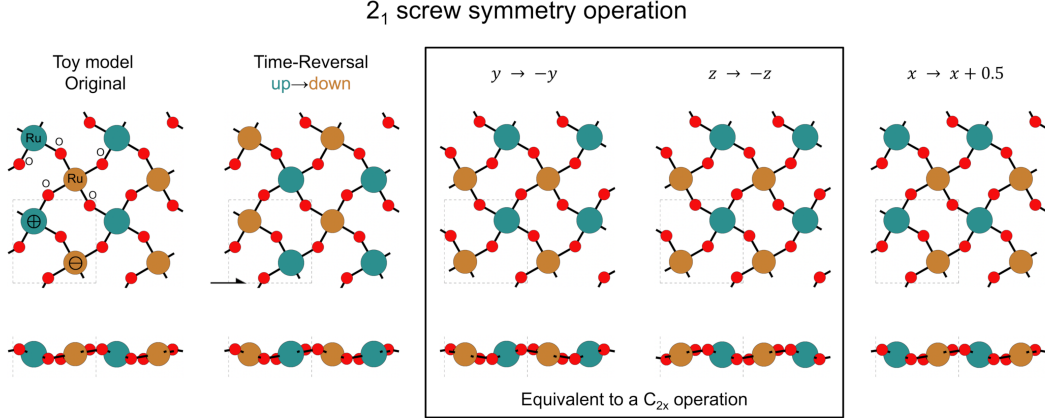


FIG. S11: Symmetry operations responsible for the altermagnetic character of the toy model. Starting from the Ru-O plane of the 2D-CRO (first panel), a time-reversal operation is applied (second panel). Subsequently, a C_{2x} operation is performed (third and fourth panels), followed by a translation in the x-direction (fifth panel).

The task now is to find a way to recover the initial configuration (first panel) by applying symmetry and translation operations on the structure affected by the time-reversal operation (second panel). After a symmetry analysis using the PYMATGEN library², we found that the 2_1 screw symmetry operation achieves this. The 2_1 screw operation can be separated into two stages: a rotation followed by a translation. The rotation corresponds to a C_{2x} operation, equivalent to the $y \rightarrow -y$ inversion followed by the $z \rightarrow -z$ inversion, shown in the third and fourth panels. Finally, a translation of half a unit cell in the x-direction allows us to recover the initial configuration, as illustrated in the fifth panel.

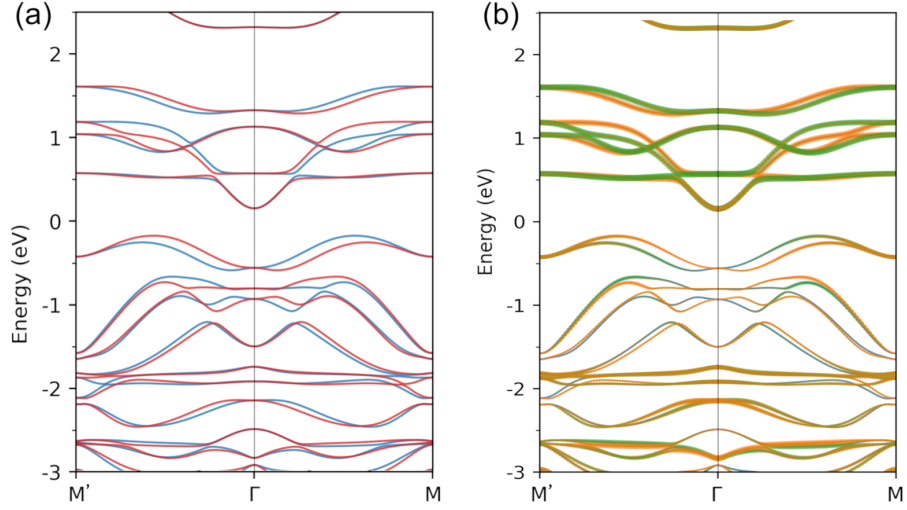


FIG. S12: (Color online) The toy model band structure. In (a), the projection of spin-up and spin-down components is shown with blue and red lines, respectively; this panel is the same as Fig. 8. In (b), the projection onto the Ru atoms is depicted, where green and orange lines represent the projections onto the two different Ru atoms.

SIX. PHONON DISPERSION BANDS

The phonon band structure (in Fig. S13) along the high-symmetry points shows no values at negative frequencies, indicating stability.

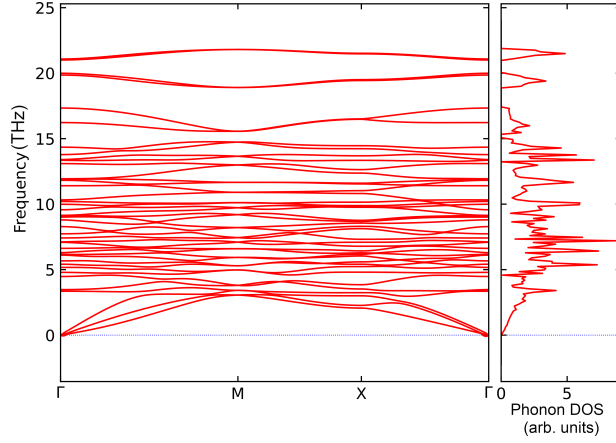


FIG. S13: Phonon dispersion bands and density of states (DOS) of 2D-CRO for $U=1$ eV. The absence of negative frequencies indicates the absence of imaginary phonon modes, confirming the mechanical stability of the system.

SX. MOLECULAR DYNAMICS

In Figure S14, energy variation and temperature evolution for a $2 \times 2 \times 1$ supercell for the 2D-CRO in FM configuration with $U = 1$ eV. The system maintains structural stability after 10 ps at 600 K, only showing small bending due to thermal agitation.

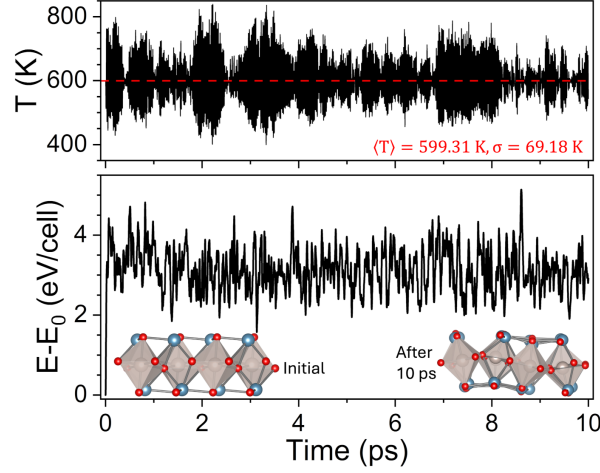


FIG. S14: (Color online) Temperature and energy variation over time in molecular dynamics simulations of the $2 \times 2 \times 1$ cell using a Nosé-Hoover thermostat at 600 K. Panel (a) shows the system temperature, and panel (b) shows the energy variation relative to the initial configuration (E_0). The inset in panel (b) depicts the initial and final geometries after 10 ps at 600 K. The observed stability in both energy and geometry confirms the dynamical stability of the monolayer at this temperature.

SXI. ELASTIC PROPERTIES

Figure S15 shows the main elastic properties of the 2D-CRO for the FM ($U = 1$ eV) and AF ($U = 2$ eV) configurations. The elastic properties exhibit angular dependence³. For the ferromagnetic configuration ($U = 1$ eV), Young's modulus varies between 41.18 N/m and 84.67 N/m, the shear modulus ranges from 16.24 N/m to 85.56 N/m, and Poisson's Ratio fluctuates between -0.51 and 0.27. In the antiferromagnetic configuration ($U = 2$ eV), Young's modulus spans from 10.91 N/m to 92.39 N/m, the shear modulus changes between 3.41 N/m and 54.05 N/m, and Poisson's Ratio shifts from -0.2 to 0.98.

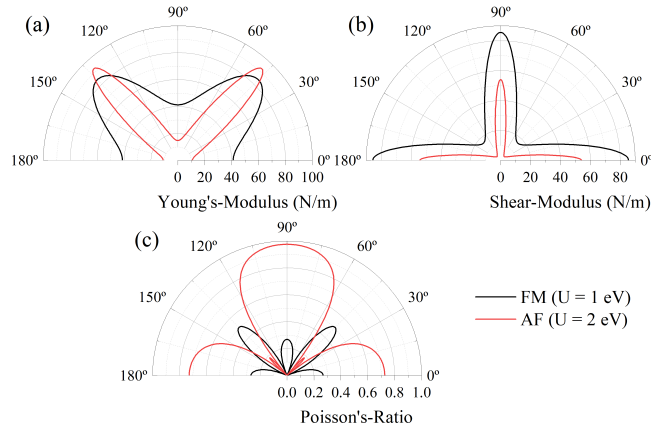


FIG. S15: (Color online) Anisotropic mechanical properties of the 2D-CRO monolayer. (a) Young's modulus, (b) shear modulus, and (c) Poisson's ratio are plotted as a function of the angle in the ab-plane. The black lines represent the ferromagnetic (FM) configuration with $U = 1$ eV, while the red lines represent the antiferromagnetic (AF) configuration with $U = 2$ eV. Note the directional dependence of the mechanical properties and the impact of different magnetic configurations on the elastic properties.

* Electronic address: jhon.gonzalez@uatonf.cl

¹ H. Nobukane, K. Yanagihara, Y. Kunisada, Y. Ogasawara, K. Isono, K. Nomura, K. Tanahashi, T. Nomura, T. Akiyama, and S. Tanda, *Scientific reports* **10**, 3462 (2020).

² S. P. Ong, W. D. Richards, A. Jain, G. Hautier, M. Kocher, S. Cholia, D. Gunter, V. L. Chevrier, K. A. Persson, and G. Ceder, *Computational Materials Science* **68**, 314 (2013).

³ V. Wang, G. Tang, Y.-C. Liu, R.-T. Wang, H. Mizuseki, Y. Kawazoe, J. Nara, and W. T. Geng, *The Journal of Physical Chemistry Letters* **13**, 11581 (2022).